

# Charge Density Wave Caused by Reducing ThSe<sub>3</sub> by One Electron. Superstructure and Short-Range Order in ATh<sub>2</sub>Se<sub>6</sub> (A = K, Rb) Studied by X-ray Diffraction, Electron Diffraction, and Diffuse Scattering

Kyoung-Shin Choi,<sup>†</sup> Rhonda Patschke,<sup>†</sup> Simon J. L. Billinge,<sup>‡</sup> Mark J. Waner,<sup>†</sup> Marcos Dantus,<sup>†</sup> and Mercouri G. Kanatzidis<sup>\*,†</sup>

Contribution from the Department of Chemistry and Department of Physics and Astronomy and Center for Fundamental Materials Research, Michigan State University, East Lansing, Michigan 48824

Received May 14, 1998

**Abstract:** The two isostructural compounds, ATh<sub>2</sub>Se<sub>6</sub> (A = K, Rb), adopt the orthorhombic space group *Immm*. ATh<sub>2</sub>Se<sub>6</sub> has a two-dimensional structure which is related to the ZrSe<sub>3</sub>-type structure with K<sup>+</sup>/Rb<sup>+</sup> cations stabilized between the layers. These compounds represent the intercalated form of ThSe<sub>3</sub> with 0.5 equiv of alkali metal ion. The stacking arrangement of the layers is slightly modified from that of ZrSe<sub>3</sub> in order to stabilize the newly introduced alkali metal ions between the layers. Electron diffraction studies reveal a static charge density wave (CDW), due to electron localization, resulting in 4a × 4b superstructure. An atomic pair distribution function analysis and spectroscopy confirmed the presence of diselenide groups in the ZrSe<sub>3</sub>-type layer (invisible by the single-crystal structure analysis) and support the notion that these Se atoms in the [Th<sub>2</sub>Se<sub>6</sub>] layers accept the extra electron from the alkali metal, and this results in breaking one out of four diselenide bonds. The superstructure is due to ordering of the three Se<sub>2</sub><sup>2-</sup> and two Se<sup>2-</sup> species along both directions. Optical absorption, Raman spectroscopy, and atomic force microscopy as well as magnetic susceptibility measurements support these conclusions.

## 1. Introduction

The reactions of lanthanides in A<sub>2</sub>Q<sub>x</sub> (A = alkali metal, Q = S, Se, Te) fluxes have led to new phases which repeat several structural motifs seen in known binary and ternary chalcogenides.<sup>1</sup> Recently, we have extended the molten salt synthetic method to thio-<sup>2</sup> and selenoantimonate fluxes which are little investigated.<sup>3,4</sup> We were attracted to the possibility of combining lanthanides and actinides with chalcoantimonate fragments because of the potentially interesting structural distortions which could develop around the Sb<sup>3+</sup> centers (due to the lone pair of electrons) and the rather large f elements.<sup>3,5,6</sup> In most cases,

depending on the flux basicity, quaternary phases were obtained at temperatures of <650 °C, while binary or ternary phases were found to be thermodynamically stable at higher temperatures. For example, the KThSb<sub>2</sub>Se<sub>6</sub><sup>3</sup> forms under such conditions, but when we attempted to prepare A/Th/Sb/Se quaternary phases at temperatures of >700 °C, phase separation occurred and instead the ternary compounds, ATh<sub>2</sub>Se<sub>6</sub> (A = K, Rb), were isolated. These compounds have a two-dimensional structure with layers that are equivalent to those seen in ZrSe<sub>3</sub><sup>7</sup> with alkali metal ions between the layers. Since ThSe<sub>3</sub> also adopts the ZrSe<sub>3</sub> structure type,<sup>8</sup> we recognized that ATh<sub>2</sub>Se<sub>6</sub> represents a well-crystallized version of intercalated ThSe<sub>3</sub> with 0.5 equiv of an alkali metal. This is significant because, normally, intercalated samples have much poorer crystallinity than the pristine parent ones. The lack of ability to perform single-crystal structure investigations in these samples leaves many of the fine structural details unresolved. Often these details are important in understanding the properties of intercalated layered materials such as the nature of intralayer guest sites for alkali ions and the effects of charge density waves on electrical conductivity, ion mobility, color, etc.

Two kinds of structural modifications of the ZrSe<sub>3</sub>-type structure are expected for the ATh<sub>2</sub>Se<sub>6</sub> compounds. The first structural modification is that of the layer itself. This layer, in which the formal charges balance as Th<sup>4+</sup>Se<sup>2-</sup>(Se<sub>2</sub><sup>2-</sup>), undergoes reduction by the alkali metal. Either the diselenide group, Se<sub>2</sub><sup>2-</sup>, or the Th<sup>4+</sup> center could act as a possible reduction sites. We

<sup>†</sup> Department of Chemistry and Center for Fundamental Materials Research.

<sup>‡</sup> Department of Physics and Astronomy and Center for Fundamental Materials Research.

(1) (a) Sutorik, A. C.; Albritton-Thomas, J.; Kannewurf, C. R.; Kanatzidis, M. G. *J. Am. Chem. Soc.* **1994**, *116*, 7706–7713. (b) Kanatzidis, M. G.; Sutorik, A. C. *Prog. Inorg. Chem.* **1995**, *43*, 151–265. (c) Sutorik, A. C.; Albritton-Thomas, J.; Hogan, T.; Kannewurf, C. R.; Kanatzidis, M. G. *Chem. Mater.* **1996**, *8*, 751–761. (d) Sutorik, A. C.; Kanatzidis, M. G. *Chem. Mater.* **1996**, *9*, 387–398.

(2) (a) Hanco, J. A.; Kanatzidis, M. G. Abstract 0413 from 210th Fall American Chemical Society Meeting, Chicago, IL, 1995. (b) Hanco, J. A.; Kanatzidis, M. G. *J. Chem. Soc., Chem. Commun.* **1998**, 725–726. (c) Hanco, J. A.; Kanatzidis, M. G. *J. Alloys Comp.*, in press.

(3) Choi, K.-S.; Iordanidis, L.; Chondroudis, K.; Kanatzidis, M. G. *Inorg. Chem.* **1997**, *36*, 3804–3805 and the references therein.

(4) Chung, D.-Y.; Choi, K.-S.; Iordanidis, L.; Schindler, J. L.; Brazis, P.; Kannewurf, C. R.; Chen, B.; Hu, S.; Uher, C.; Kanatzidis, M. G. *Chem. Mater.* **1997**, *9*, 3060–3071.

(5) K<sub>2</sub>Gd<sub>2</sub>Sb<sub>2</sub>Se<sub>9</sub> and K<sub>2</sub>La<sub>2</sub>Sb<sub>2</sub>Se<sub>9</sub>; Choi, K.-S.; Hanco, J. A.; Kanatzidis, M. G. Submitted for publication.

(6) KU<sub>2</sub>SbSe<sub>8</sub> and RbU<sub>2</sub>SbS<sub>8</sub>; Choi, K.-S.; Kanatzidis, M. G. Manuscript in preparation.

(7) Krönert, Von W.; Plieth, K. *Z. Anorg. Allg. Chem.* **1965**, *336*, 207–218.

(8) Noël, H. *J. Inorg. Nucl. Chem.* **1980**, *42*, 1715–1717.

wanted to investigate where and how the layers could accommodate the extra electrons from the alkali metal and how the presence of these electrons influences the  $ZrSe_3$ -type structure. In fact, this system has a lot of similarity to the Li-intercalated  $ZrSe_3$ , which has been extensively investigated for possible battery applications. With  $Li_xZrSe_3$  ( $0 < x \leq 3$ ),<sup>9</sup> there is still uncertainty about the intercalation mechanism, the local environment of the Li ion, and the structural change of the host material during the intercalation process. In this respect, our study on  $A_xThSe_3$  ( $x = 0.5$ ;  $A = K, Rb$ ) could shed new light on the intercalation process of Li in  $ZrSe_3$ -type compounds by providing structural insight as to how the host structure responds when electrons are inserted into it. The second type of structural modification is attributed to the stacking arrangement of the layers. In  $ZrSe_3$ , the stacking arrangement of the layers produces trigonal prismatic sites between the layers. These sites, however, are not large enough to accommodate the  $K^+/Rb^+$  ions. Therefore, the layers must stack in such a way that they can provide enough space for the newly introduced alkali metals.

One of these compounds,  $KTh_2Se_6$ , was reported<sup>10</sup> while this manuscript was in preparation. Only the space group of this compound was mentioned, without complete characterization of the structure or physical properties, and it was concluded that  $KTh_2Se_6$  is isostructural with  $KTh_2Te_6$ <sup>10</sup> and  $CsTh_2Te_6$ <sup>11</sup> on the basis of the unit cell parameters and the systematic absences determined by oscillation and Weissenberg photographs. However, according to our results,  $KTh_2Se_6$  is crystallographically different from that of  $KTh_2Te_6$ . The known difference between selenium and tellurium to engage in chalcogen-chalcogen interactions does not allow  $ATH_2Se_6$  ( $A = K, Rb$ ) to have the exact same stacking arrangement of the anionic layers and cations as  $KTh_2Te_6$ , even though their compositions and basic frameworks [ $Th_2Q_6$ ] ( $Q = Se, Te$ ) are the same. In fact, it is instructive to compare these two structures and understand why the selenide adopts a slightly different structure.

Here we report a complete structural study of  $ATH_2Se_6$  ( $A = K, Rb$ ) and discuss it with respect to the structures of  $ZrSe_3$  and  $KTh_2Te_6$ . In addition to a single-crystal X-ray crystallographic analysis which gives the average structure, electron diffraction studies on  $ATH_2Se_6$  have revealed a subtle, but significant, structural modification which originates from an electronic instability caused by the extra electrons added on the  $ThSe_3$  framework. With the aid of Raman and optical spectroscopy as well as magnetic susceptibility measurements, we suggest that this structure distortion is due to the reductive cleavage of one-quarter of the total diselenide groups in the lattice and represents a charge density wave (CDW) on the ideal structure of  $ThSe_3$ .<sup>12</sup> In addition, we also carried out an atomic pair distribution function (PDF) analysis of the X-ray diffuse scattering generated by  $KTh_2Se_6$  to probe the local structure

(9) Sourisseau, C.; Gwet, S. P.; Gard, P. J. *Solid State Chem.* **1988**, *72*, 257–271 and references therein.

(10) Wu, E. J.; Pell, M. A.; Ibers, J. A. *J. Alloys Comp.* **1997**, *255*, 106–109.

(11) Cody, J. A.; Ibers, J. A. *Inorg. Chem.* **1996**, *16*, 3273–3277.

(12) Found primarily in one- and two-dimensional metallic compounds, the CDW state is characterized by a periodic density wave appearing in the conduction electron density and a concomitant periodic superstructure of a longitudinal lattice-distortion wave. The properties of CDW systems have been studied extensively during the past 25 years, mostly in di- and trichalcogenides such as  $TaS_2$  and  $NbSe_3$ . A large fraction of this research has been devoted to studies of the nonlinear electronic transport exhibited by CDW systems and the nature of the superstructure. For comprehensive reviews of the electronic properties of CDW systems, see: (a) Monceau, P. *Electronic Properties of Quasi-One-Dimensional Materials*; Reidel: Dordrecht, The Netherlands, 1985; Part II, p 139. (b) Grüner, G. *Rev. Mod. Phys.* **1998**, *60*, 1129 and references therein.

around the diselenide group. This verified the structure distortion and the presence of short Se–Se bonds, which are “invisible” by the single-crystal X-ray crystallographic analysis.

## 2. Experimental Section

**2.1. Synthesis.** The following reagents were used as obtained: Thorium, 100 mesh, Cerac, Milwaukee, WI; selenium powder, 100 mesh, Aldrich, Milwaukee, WI; potassium metal, analytical reagent, Mallinckrodt Inc., Paris, KY; rubidium metal, analytical reagent, Johnson Matthey, Ward Hill, MA. The  $K_2Se/Rb_2Se$  starting materials were prepared by a stoichiometric reaction of potassium/rubidium metal and selenium in liquid  $NH_3$ .

**$ATH_2Se_6$  ( $A = K, Rb$ ).** These compounds were synthesized from a mixture of 0.1256 g (0.80 mmol) of  $K_2Se$  (or 0.200 g (0.80 mmol) of  $Rb_2Se$  for  $RbTh_2Se_6$ ), 0.1856 g (0.80 mmol) of Th, 0.3158 g (0.40 mmol) of Sb, and 0.4158 g (4.0 mmol) of Se. These reagents were thoroughly mixed, sealed in a carbon-coated fused silica tube (9 mm diameter), and heated at 720 °C for 5 days (cooling 2 °C/h). Pure golden-black planks of  $ATH_2Se_6$  were obtained by isolation in degassed dimethylformamide (DMF) (>90% yield based on Th). The compositions of the materials were analyzed by scanning electron microscope (SEM)/energy dispersive spectroscopy (EDS). No Sb impurities were detected in the compounds. Homogeneity was confirmed by comparing the powder X-ray diffraction pattern of the product against one calculated using X-ray single-crystal data. It is interesting to note that, even though the Sb was not incorporated into the compound, it is needed to grow large crystals of this material in high yield by forming a suitable  $ASb_xSe_y$  ( $A = K, Rb$ ) flux. Other reaction mixtures without Sb did not give as pure products or as large crystals as the ones obtained from the  $ASb_xSe_y$  fluxes. The reactions at lower temperature (< 700 °C) gave a lower yield of the compounds.

**2.2. Physical Measurements. Semiquantitative Microprobe Analyses.** The analyses were performed using a JEOL JSM-35C scanning electron microscope (SEM) equipped with a Tracor Northern energy dispersive spectroscopy (EDS) detector. Data were acquired on several crystals using an accelerating voltage of 20 kV and 40-s accumulation time.

**Solid-State UV/Vis Spectroscopy.** Optical diffuse reflectance measurements were performed at room temperature with a Shimadzu UV-3101 PC double-beam, double-monochromator spectrophotometer operating in the 200–2500-nm region. The instrument is equipped with an integrating sphere and controlled by a personal computer.  $BaSO_4$  was used as a 100% reflectance standard for all materials. Samples were prepared by grinding them to a fine powder, spreading them on a compacted surface of the powdered standard material, and preloading them into a sample holder. The reflectance versus wavelength data generated were used to estimate the material's band gap by converting the reflectance data to absorption data as described elsewhere.<sup>13</sup>

**Raman Spectroscopy.** Raman spectra of the crystal specimens were recorded on a Holoprobe Raman spectrograph equipped with a 633-nm HeNe laser and a CCD camera detector. The instrument was coupled to an Olympus BX60 microscope. The spot size of the laser beam was 10  $\mu m$  when a 50 $\times$  objective lens was used.

**Magnetic Susceptibility.** The magnetic response of the compound was measured over the range 2–300 K using a MPMS Quantum Design SQUID magnetometer. Samples were ground to a fine powder to minimize possible anisotropic effects and loaded into PVC containers. The temperature-dependent susceptibility measurements were performed at 1000 G. Corrections for the diamagnetism of the sample containers were made by measuring the magnetic response of the empty container at the same magnetic field that was used for the filled container. The core diamagnetic contribution of every ion to  $\chi_m$  was subtracted according to Selwood.<sup>14</sup>

**Differential Thermal Analysis (DTA).** DTA experiments were performed on a computer-controlled Shimadzu DTA-50 thermal analyzer. Typically, a sample (~20 mg) of ground crystalline material

(13) McCarthy, T. J.; Ngeyi, S.-P.; Liao J.-H.; Degroot, D.; Hogan, T.; Kannewurf, C. R.; Kanatzidis, M. G. *Chem. Mater.* **1993**, *5*, 331–340.

(14) Selwood, P. W. *Magnetochemistry*, 2nd ed.; Interscience Publishers: New York, 1956; p 78.

was sealed in a quartz ampule under vacuum. A quartz ampule of equal mass filled with  $\text{Al}_2\text{O}_3$  was sealed and placed on the reference side of the detector. The samples were heated to the desired temperature at  $5^\circ\text{C}/\text{min}$  and isothermed for 10 min, followed by cooling at  $-5^\circ\text{C}/\text{min}$  to  $50^\circ\text{C}$ . The stability and reproducibility of the samples were monitored by running multiple heating/cooling cycles. Residues of the DTA experiments were examined by X-ray powder diffraction.

**2.3. X-ray Crystallography.** Single crystals of  $\text{KTh}_2\text{Se}_6$  with dimensions  $0.41 \times 0.04 \times 0.06$  mm and of  $\text{RbTh}_2\text{Se}_6$  with dimensions of  $0.29 \times 0.13 \times 0.03$  mm were mounted on the tip of a glass fiber. Intensity data for  $\text{KTh}_2\text{Se}_6$  were collected at room temperature on a Rigaku AFC6S four-circle automated diffractometer equipped with a graphite-crystal monochromator. The unit cell parameters were determined from a least-squares refinement using the setting angles of 20 carefully centered reflections in the  $8^\circ \leq 2\theta \leq 30^\circ$  range. The data were collected with the  $\omega$  scan technique over a full sphere of reciprocal space, up to  $50^\circ$  in  $2\theta$ . Crystal stability was monitored with three standard reflections whose intensities were checked every 150 reflections. No significant decay was observed during the data collection period. An empirical absorption correction was applied on the basis of  $\psi$  scans. Since the cell parameters given by the four-circle automated diffractometer had high standard deviations, Guinier X-ray powder diffraction patterns (calibrated with a Si standard) were used to obtain more precise cell parameters for  $\text{KTh}_2\text{Se}_6$ . LATCON in Xtal3.2 software<sup>15</sup> was used to refine the cell parameters with 38 reflections selected in the  $13^\circ \leq 2\theta \leq 44^\circ$  range, and the resultant values were used for the calculation of bonds and angles.

The crystallographic data for  $\text{RbTh}_2\text{Se}_6$  were collected at 173.1 K on a Siemens SMART Platform CCD diffractometer using graphite monochromatized Mo  $K\alpha$  radiation. The data were collected over a full sphere of reciprocal space, up to  $56^\circ$  in  $2\theta$ . The individual frames were measured with an  $\omega$  rotation of  $0.3^\circ$  and an acquisition time of 25 s. The SMART<sup>16</sup> software was used for the data acquisition and SAINT<sup>17</sup> for the data extraction and reduction. The absorption correction was performed using SADABS.<sup>18</sup> The complete data collection parameters and details of the structure solution and refinement for both compounds are given in Table 1.

Structure solutions and refinements were performed, for both compounds, using the SHELXTL<sup>19</sup> package of crystallographic programs. Systematic absence conditions of the data sets gave three possible acentric space groups,  $I222$  (no. 23),  $I2_12_12_1$  (no. 24),  $Immm$  (no. 34), and one centric space group,  $Immm$  (no. 71). The MISSYM algorithm<sup>20</sup> as implemented in the PLATON program<sup>21</sup> revealed a center of inversion in the structure, suggesting that the correct space group is  $Immm$ . The space group reported for  $\text{KTh}_2\text{Se}_6$  earlier was  $Cmcm$ <sup>10</sup> because it was assumed that  $\text{KTh}_2\text{Se}_6$  was isostructural with  $\text{KTh}_2\text{Te}_6$ , which crystallizes in this space group. The only evidence that led these authors to this conclusion was two systematic absence conditions ( $hkl$ ,  $h + k = 2n + 1$ ;  $h0l$ ,  $l = 2n + 1$ ) obtained from oscillation and Weissenberg photographs. These two conditions, however, are not sufficient enough evidences to conclude the correct space group because they are also subconditions of  $I$  centering ( $hkl$ ,  $h + k + l = 2n + 1$ ). As a matter of fact, we found that 912 reflections out of the 1812 total reflections collected for  $\text{KTh}_2\text{Se}_6$  violate the systematic absence conditions of  $Cmcm$  such as  $hkl$ ,  $h + k = 2n + 1$ ;  $0kl$ ,  $k = 2n + 1$ ;  $h0l$ ,  $h, l = 2n + 1$ , etc. Nevertheless, we still tried to refine the structure using the atomic coordinates reported for the  $Cmcm$  space group. This gave a significantly higher values of  $R1 = 0.0876$  and  $wR2 = 0.1860$  for all data. In addition, the isotropic temperature factor for the  $\text{K}^+$  ions, which are equally disordered over two crystallographically

**Table 1.** Summary of Crystallographic Data and Structural Analysis for  $\text{KTh}_2\text{Se}_6$  and  $\text{RbTh}_2\text{Se}_6$

formula	$\text{KTh}_2\text{Se}_6$	$\text{RbTh}_2\text{Se}_6$
formula weight	976.94	1023.31
crystal habit	golden-black needle	golden-black plate
space group	$Immm$ (no. 71)	$Immm$ (no. 71)
$a$ , Å	4.1899(5)	4.2031(1)
$b$ , Å	5.6337(5)	5.6347(1)
$c$ , Å	21.860(4)	22.4714(1)
$Z$ ; $V$ , Å <sup>3</sup>	2; 516.01(13)	2; 532.19(2)
$D_{\text{calc}}$ , g/cm <sup>3</sup>	6.288	6.386
temp, K	298	173
$\lambda(\text{Mo } K\alpha)$ , Å	0.71073	0.71073
$\mu(\text{Mo } K\alpha)$ , cm <sup>-1</sup>	502.74	528.98
$F(000)$	806	842
$2\theta_{\text{max}}$ , deg	50.0	56.5
total no. of data	1812	2822
measd		
no. of unique data	296 [ $R(\text{int}) = 0.0399$ ]	420 [ $R(\text{int}) = 0.0960$ ]
no. of variables	19	19
refinement method	full-matrix least-squares on $F^2$	
final $R$ indices <sup>a,b</sup>	$R1 = 0.0212$	$R1 = 0.0390$
$[I > 2\sigma]$	$wR2 = 0.0528$	$wR2 = 0.0875$
$R$ indices (all data) <sup>a,b</sup>	$R1 = 0.0239$	$R1 = 0.0405$
	$wR2 = 0.0564$	$wR2 = 0.0880$
goodness of fit on $F^2$	1.120	1.112

$$^a R1 = \sum ||F_o| - |F_c|| / \sum |F_o|. \quad ^b wR2 = \{ \sum [w(F_o^2 - F_c^2)^2] / \sum [w(F_o^2)^2] \}^{1/2}$$

**Table 2.** Fractional Atomic Coordinates and Equivalent Isotropic Displacement Parameters ( $U_{\text{eq}}$ ) Values for  $\text{KTh}_2\text{Se}_6$  and  $\text{RbTh}_2\text{Se}_6$  with Estimated Standard Deviations in Parentheses

atom	$x$	$y$	$z$	$U_{\text{eq}}^a$ , Å <sup>2</sup>
$\text{KTh}_2\text{Se}_6$				
Th	1/2	0	0.3225(1)	0.010(1)
Se(1)	0	0.2420(2)	0.3976(1)	0.020(1)
Se(2)	0	0	0.2267(1)	0.010(1)
K	0	0	0	0.030(1)
$\text{RbTh}_2\text{Se}_6$				
Th	1/2	0	0.3204(1)	0.006(1)
Se(1)	0	0.2421(2)	0.3936(1)	0.015(1)
Se(2)	0	0	0.2273(1)	0.005(1)
Rb	0	0	0	0.016(1)

<sup>a</sup>  $U_{\text{eq}}$  is defined as one-third of the trace of the orthogonalized  $U_{ij}$  tensor.

equivalent sites in the  $Cmcm$  space group, was very large ( $U_{\text{eq}} = 0.398$ ). The structure was solved and refined successfully using the  $Immm$  space group with  $R$  indices shown in Table 1. The coordinates of all atoms, average temperature factors, and their estimated standard deviations are given in Table 2.

**2.4. Electron Diffraction Study (TEM).** Electron crystallographic studies were carried out on a JEOL 100CX transmission electron microscope (TEM) using an electron beam generated by a  $\text{CeB}_6$  filament and an acceleration voltage of 120 kV. After the samples were ground to a fine powder in acetone, the specimens were prepared by dipping a carbon coated copper grid in the suspension. The samples showed no decomposition under the electron beam.

**2.5. Pair Distribution Function Analysis (PDF).** The procedures used to perform atomic pair distribution function analysis of X-ray diffraction data have been published elsewhere.<sup>22,23</sup> Powder diffraction data were collected out to  $2\theta_{\text{max}}$  of  $140^\circ$  on an in-house powder diffractometer in Bragg-Brentano geometry using Mo  $K\alpha$  radiation.

**2.6. Atomic Force Microscopy (AFM).** Contact AFM images were acquired using a Park Scientific Instruments Autoprobe CP scanning probe microscope, with a  $5\text{-}\mu\text{m}$  high-resolution scanner. Microlever cantilevers (Park Scientific Instruments) having a spring constant of approximately 0.5 N/m and an integrated silicon nitride probe with a radius of curvature of approximately 50 nm, according to

(22) Warren, B. E. *X-ray Diffraction*; Dover: New York, 1990.

(23) (a) Egami, T. *Mater. Trans.* **1990**, *31*, 163. (b) Billinge S. J. L.; Egami, T. *Phys. Rev. B* **1993**, *47*, 14386.

(15) Hall, S. R., Flack, H. D., Stewart, J. M., Eds. *Xtal3.2 Reference Manual*; University of Western Australia: Australia, Geneva, Switzerland, and Maryland, 1992.

(16) SMART: Siemens Analytical X-ray Systems, Inc., Madison, WI, 1994.

(17) SAINT, Version 4:—Siemens Analytical X-ray Systems, Inc., Madison, WI, 1994–1996.

(18) Sheldrick, G. M. University of Göttingen, Germany, to be published.

(19) Sheldrick, G. M. *SHELXTL*, Version 5; Siemens Analytical X-ray Systems, Inc.: Madison, WI, 1994.

(20) Le Page, Y. *J. Appl. Crystallogr.* **1987**, *20*, 264–269.

(21) Spek, A. L. *Acta Crystallogr., Sect. A* **1990**, *46*, C34.

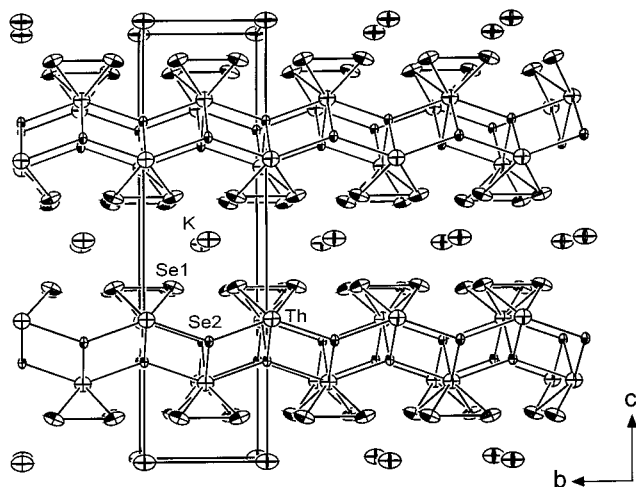


**Figure 1.** ORTEP representation and labeling of  $\text{KTh}_2\text{Se}_6$  viewed down the  $c$  axis with 90% thermal vibrational ellipsoids. The labeling scheme for the  $\text{RbTh}_2\text{Se}_6$  is analogous.

the manufacturer, were used. The experiment was conducted in air using either pristine (as made) or a freshly cleaved surfaces of single crystals of  $\text{RbTh}_2\text{Se}_6$ .

The AFM data were recorded in constant height mode under controlled ambient conditions (35% humidity and 21 °C). In this mode of imaging the deflection of the cantilever is measured as the sample is raster scanned beneath the tip. The force used to acquire these images was 10 nN. The samples were scanned at a rate of 32 lines per second. Each image was 100–150 Å and 512 × 512 pixels. Distances were calibrated using the 5.1-Å lattice spacing obtained from freshly cleaved muscovite mica.<sup>24</sup>

### 3. Results and Discussion

**Structure.**  $A\text{Th}_2\text{Se}_6$  ( $A = \text{K}, \text{Rb}$ ) has a two-dimensional structure composed of infinite  $[\text{Th}_2\text{Se}_6]^-$  layers that lie perpendicular to the  $[001]$  direction, see Figure 1. The Th atoms in this layer are coordinated by eight Se atoms in a distorted bicapped trigonal prismatic geometry. Each trigonal prism has two edges much shorter than the rest. These short edges are formed by the diselenide groups,  $\text{Se}_2^{2-}$ . The Th-centered trigonal prisms make one-dimensional chains parallel to the  $[100]$  direction by sharing triangular faces with each other. The layers are formed when each chain shares monoselenide ions,  $\text{Se}^{2-}$ , at the apex and capping sites with neighboring chains.

Each  $[\text{Th}_2\text{Se}_6]^-$  layer itself can be described as  $\text{ZrSe}_3$  type except for the stacking arrangement of the layers. In  $\text{ZrSe}_3$ , all Se atoms of the diselenide groups in one layer are staggered with the corresponding Se atoms in the next layer to minimize the steric repulsion, see Figure 2a. The only reasonable place for the alkali metal to reside between the layers are trigonal prismatic sites, the size of which is not big enough to accommodate the  $\text{K}^+/\text{Rb}^+$  ions. Therefore, in  $A\text{Th}_2\text{Se}_6$  ( $A = \text{K}, \text{Rb}$ ), all the  $[\text{Th}_2\text{Se}_6]^-$  layers are stacked in an eclipsed fashion by shifting every other layer one-fourth along the  $b$  axis to generate larger square prismatic sites. Since the crystallographically observed Se–Se distance in the diselenide bond is 2.727(2) Å for  $\text{KTh}_2\text{Se}_6$  (2.728(3) Å for  $\text{RbTh}_2\text{Se}_6$ ) and the shortest distance between the diselenide groups is 2.907(2) Å, (2.907(3) for  $\text{RbTh}_2\text{Se}_6$ ), the resultant stacking arrangement generates two square prismatic sites with different sizes, see Figure 2b. The  $\text{K}^+/\text{Rb}^+$  ions are stabilized in the larger square prismatic site and are coordinated by eight Se atoms, with K - -

Se distances of 3.3922(9) Å for  $\text{KTh}_2\text{Se}_6$  and  $\text{Rb}^+\cdots\text{Se}$  distances of 3.4989(9) Å for  $\text{RbTh}_2\text{Se}_6$ .

In  $\text{KTh}_2\text{Te}_6$ , the Te–Te distance within the ditelluride fragment (3.057(3) Å) is very similar to the Te–Te distance between ditelluride fragments (3.085(3) Å). Considering that tellurium is more basic and softer than selenium, the electrons on the Te atoms can easily delocalize to neighboring Te atoms, giving rise to, essentially, infinite chains along the  $[010]$  direction. In this case, the eclipsed stacking of the ditelluride fragment of the  $[\text{Th}_2\text{Te}_6]^-$  layers is no longer preferred to make suitable pockets for the alkali metal (Figure 2c). Therefore,  $\text{KTh}_2\text{Te}_6$  adopts a slightly different stacking arrangement of layers by staggering the ditelluride units of one layer to those of the next layer. All square prismatic sites between the layers are still present but are of equal size which is suitable to accommodate the  $\text{K}^+$  ions, thus resulting in statistical disorder of the cations over all such sites.

The assignment of formal oxidation states in these phases appears to be  $\text{Th}^{4+}\text{Se}_2^{2-}(\text{Se}_2^{2.5-})$ , judging from the results of the single-crystal X-ray diffraction analysis. We find it rather unusual that the observed Se–Se distance in the diselenide bond of  $A\text{Th}_2\text{Se}_6$  is significantly longer at 2.727 Å than the normal Se–Se bond distance of  $\sim 2.35$  Å, suggesting that the oxidation state of Se(1) in the diselenide group of  $[\text{Th}_2\text{Se}_6]^-$  is between  $-1$  and  $-2$ , namely,  $-1.25$ . In other words, it would seem that the 0.5 equiv of electrons from the alkali metal is located on all the Se(1) atoms in the diselenide groups, and this elongates the Se–Se bond by 0.4 Å. This corresponds to 0.5 electron per Se–Se bond, which would give essentially partially broken bonds. This situation could cause paramagnetism in the compounds.

**Properties.** The optical properties of the compounds were determined by measuring the solid-state UV/vis diffuse reflectance spectra, which show the presence of two abrupt optical transitions at 0.90 and 2.16 eV for  $\text{KTh}_2\text{Se}_6$  and 0.90 and 2.09 eV for  $\text{RbTh}_2\text{Se}_6$ , suggesting that the materials are semiconductors and the extra electrons introduced into the  $\text{ZrSe}_3$ -type layer are localized (see Figure 3). The origin of the two transitions is not clear, but they are also present (at slightly different energies) in  $\text{ThSe}_3$  itself.<sup>25</sup> One possibility is that they are dichroic due to the anisotropic nature of the electronic band structure given the lamellar nature of these materials. In fact visual inspection of the crystals does suggest the presence of dichroism.

DTA measurements show that  $\text{KTh}_2\text{Se}_6$  and  $\text{RbTh}_2\text{Se}_6$  do not melt below 1000 °C.

The Raman spectra display shifts at  $\sim 124$ ,  $\sim 160$ ,  $\sim 199$ , and  $\sim 234$   $\text{cm}^{-1}$  for both compounds (Figure 4). Since the Se–Se stretching should appear at a higher energy than any Th–Se stretching, the absorption at  $\sim 234$   $\text{cm}^{-1}$  for  $A\text{Th}_2\text{Se}_6$  can be tentatively assigned to the diselenide group. The wavenumber at which the stretching vibrations of a normal Se–Se bond occur varies depending upon both the local geometry of the selenium atom and the metal with which it makes bonds. For example, that of  $\text{USe}_3$ <sup>26</sup> appears at  $\sim 285$   $\text{cm}^{-1}$ ,<sup>27,28</sup> that of  $\text{K}_2\text{Se}_2$  at  $\sim 253$   $\text{cm}^{-1}$ ,<sup>29</sup> and that of crystalline Se near 238  $\text{cm}^{-1}$ .<sup>28</sup> This frequency variation occurs despite the fact that the Se–Se

(25) Choi, K.-S.; Kanatzidis, M. G. Unpublished work.

(26) Ben Salem, A.; Meerschaut, A.; Rouxel, J. *C. R. Acad. Sci., Paris* **2** **1984**, 299, 617–619.

(27) Nouvel, G.; Zwick, A.; Renucci, M. A.; Lockwood, D. J.; Noël, H. *J. Phys. C: Solid State Phys.* **1987**, 20, 1881–1897.

(28) Nouvel, G.; Zwick, A.; Renucci, M. A. *J. Less-Common Met.* **1986**, 121, 253–259.

(29) Böttcher, P.; Getzschmann, J.; Keller, R. *Z. Anorg. Allg. Chem.* **1993**, 619, 476–488.

(24) Sharp, T. G.; Oden, P. I.; Buseck, P. R. *Surf. Sci. Lett.* **1993**, 284, L405–L410.

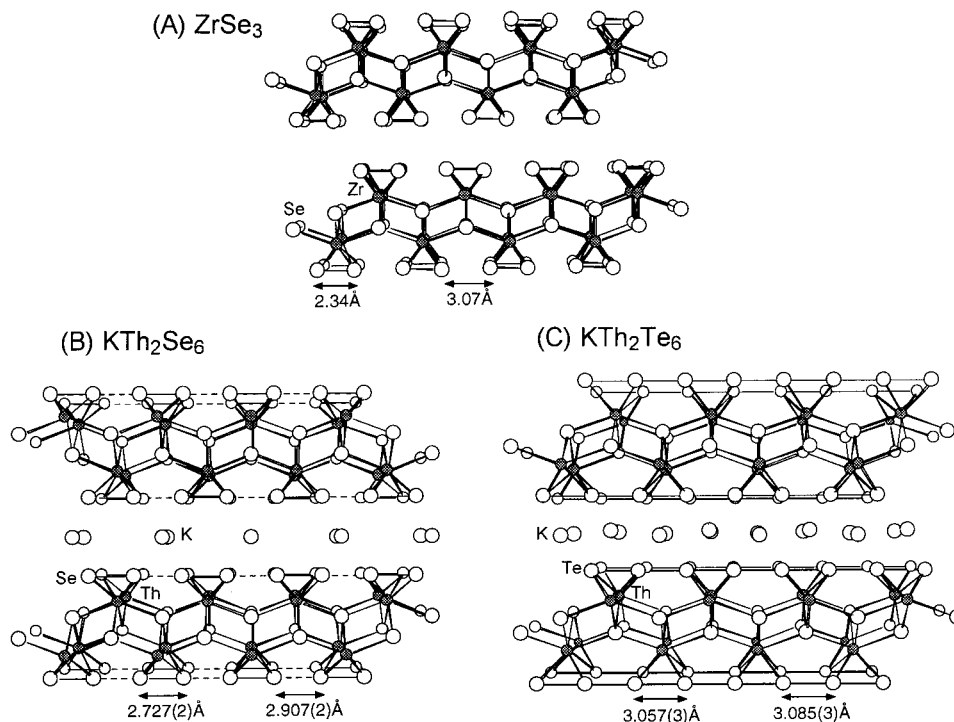


**Figure 2.** Schematic comparison of the structures of (A)  $\text{ZrSe}_3$ , (B)  $\text{KTh}_2\text{Se}_6$ , and (C)  $\text{KTh}_2\text{Te}_6$ . In  $\text{KTh}_2\text{Te}_6$ , each  $\text{K}^+$  site is half occupied.<sup>10</sup> The distribution of chalcogen–chalcogen distances are indicated.

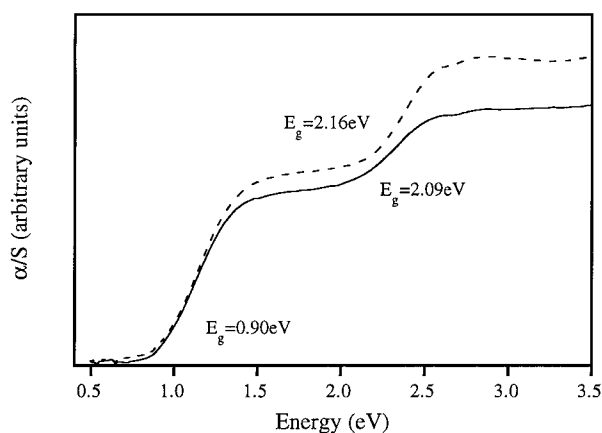


**Figure 3.** Electronic absorption spectra of  $\text{KTh}_2\text{Se}_6$  (---) and  $\text{RbTh}_2\text{Se}_6$  (—). The band gap energies,  $E_g$ , are indicated.

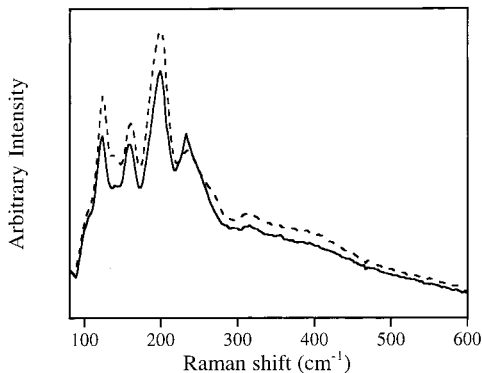


**Figure 4.** Raman spectra of  $\text{KTh}_2\text{Se}_6$  (---) and  $\text{RbTh}_2\text{Se}_6$  (—).

distance in all three compounds ranges narrowly between 2.33 and 2.40 Å. On the basis of the crystallographically observed Se–Se distance of 2.73 Å, which is lengthened by 0.35 Å, we expect the Se–Se stretching vibration to appear at much lower energy. The Raman shift at  $\sim 234 \text{ cm}^{-1}$  for  $\text{ATh}_2\text{Se}_6$ , therefore,

is inconsistent with the presence of a 2.73 Å Se–Se bond and more indicative of normal diselenide groups (i.e., with a bond distance close to 2.35 Å).

The magnetic susceptibility of  $\text{RbTh}_2\text{Se}_6$  was measured from 2 to 300 K at 1000 G, and the material appears to be diamagnetic. This is also discrepant with the model from the X-ray diffraction study, which suggests paramagnetic behavior if an unpaired electron is assumed on every  $\text{Se}_2^{2-}$  group.

These apparent inconsistencies between the spectroscopic data and the structural model suggest that the local structure associated with the Se–Se unit is more complicated than depicted from the X-ray crystallographic results. Therefore, we proceeded to examine the structure of  $\text{ATh}_2\text{Se}_6$  in greater detail using other methods such as electron diffraction, atomic force microscopy, and X-ray diffuse scattering analysis.

#### Electron Diffraction Study and Superstructure Model.

Despite the good structural refinement of the single-crystal X-ray diffraction data, we noticed that one of the anisotropic temperature factors,  $U_{22}$  for Se(1) belonging to the diselenide group, was relatively high compared with that of Se(2) and Th atoms for both the K and Rb compounds (See Table 3). This factor is three times larger than  $U_{11}$  and  $U_{33}$  for Se(1). Notice that the K/Rb atoms also have relatively high  $U_{22}$  values, which is not surprising because the alkali atoms are surrounded by Se(1) atoms and their temperature displacement factors are directly affected by the behavior of Se(1). This fact gave us a clue for the potential presence of a superstructure, along the  $b$  axis, due to positional long-range ordering of Se(1) atoms in the diselenide groups brought about by electronic coupling and resulting in a charge density wave. The fractional oxidation states for Se(1) derived from the structure determination above, in fact, makes this system a potential candidate for CDW as has been observed in other systems where similar structure/oxidation state relationships exist, e.g.  $\text{LnSe}_3$ ,  $\text{LnTe}_3$  (Ln = rare earth),  $\text{K}_{0.333}\text{Ba}_{0.667}\text{AgTe}_2$ .<sup>30</sup>

The possibility for superstructure was examined by transmission electron microscopy (TEM). Electron beams interact more

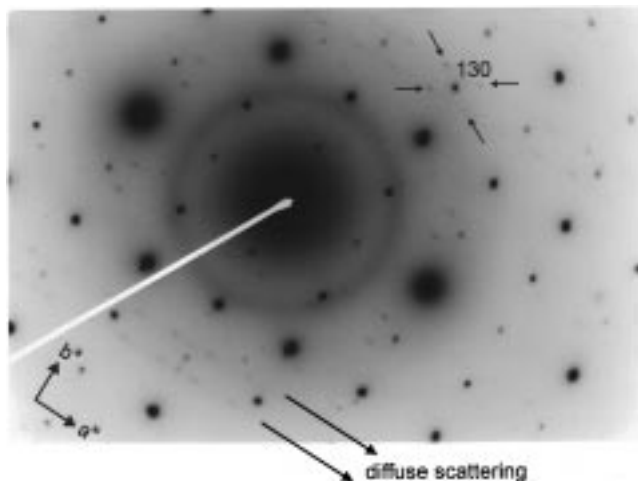
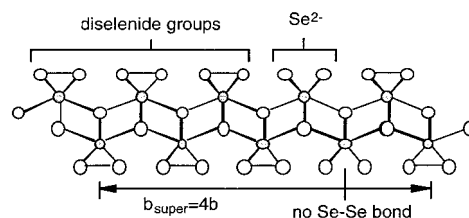
**Table 3.** Anisotropic Displacement Parameters ( $\text{\AA}^2$ ) for  $\text{KTh}_2\text{Se}_6$  and  $\text{RbTh}_2\text{Se}_6$  with Estimated Standard Deviations in Parentheses

$\text{KTh}_2\text{Se}_6$				
	Th	Se(1)	Se(2)	K
$U_{11}$	0.010(1)	0.012(1)	0.012(1)	0.024(3)
$U_{22}$	0.006(1)	0.032(1)	0.005(1)	0.042(3)
$U_{33}$	0.015(1)	0.016(1)	0.012(1)	0.022(3)
$U_{12}$	0.0000	-0.008(1)	0.0000	0.0000
$U_{13}$	0.0000	0.0000	0.0000	0.0000
$U_{23}$	0.0000	0.0000	0.0000	0.0000
$\text{RbTh}_2\text{Se}_6$				
	Th	Se(1)	Se(2)	Rb
$U_{11}$	0.005(1)	0.006(1)	0.006(1)	0.012(1)
$U_{22}$	0.003(1)	0.028(1)	0.002(1)	0.026(1)
$U_{33}$	0.010(1)	0.011(1)	0.006(1)	0.010(1)
$U_{12}$	0.0000	-0.007(1)	0.0000	0.0000
$U_{13}$	0.0000	0.0000	0.0000	0.0000
$U_{23}$	0.0000	0.0000	0.0000	0.0000

**Table 4.** Selected Distances ( $\text{\AA}$ ) and Bond Angles (deg) for  $\text{ATH}_2\text{Se}_6$  (A = K, Rb) with Standard Deviations in Parentheses

	$\text{KTh}_2\text{Se}_6$	$\text{RbTh}_2\text{Se}_6$
Bond Distances		
Th-Se(1)	2.9913(9) $\times$ 4	2.9970(9) $\times$ 4
Th-Se(2)	2.9615(11) $\times$ 2	2.9658(10) $\times$ 2
Th-Se(2)	3.0153(6) $\times$ 2	3.0147(5) $\times$ 2
A-Se(1)	3.3922(9) $\times$ 8	3.4989(9) $\times$ 8
Se(1)-Se(1)	2.727(2)	2.728(3)
Bond Angles		
Se(1)-Th-Se(1)	88.91(3) $\times$ 2	89.05(3) $\times$ 2
Se(1)-Th-Se(1)	54.23(4) $\times$ 2	54.14(5) $\times$ 2
Se(1)-Th-Se(1)	113.36(4) $\times$ 2	113.43(4) $\times$ 2
Se(2)-Th-Se(2)	75.39(2) $\times$ 4	75.46(2) $\times$ 4
Se(2)-Th-Se(2)	90.04(4)	89.05(3)
Se(2)-Th-Se(2)	138.20(6)	138.30(5)
Se(1)-Th-Se(2)	76.71(3) $\times$ 4	76.70(3) $\times$ 4
Se(1)-Th-Se(2)	128.45(2) $\times$ 4	128.36(2) $\times$ 4
Se(1)-Th-Se(2)	152.09(2) $\times$ 4	152.14(3) $\times$ 4
Se(1)-Th-Se(2)	83.85(3) $\times$ 4	83.71(2) $\times$ 4

strongly with matter than X-rays, and thus electron diffraction is more sensitive to the presence of a weak structure modulation. Indeed, electron diffraction studies revealed a weak superstructure along both the  $a$  and the  $b$  axes. Both compounds,  $\text{KTh}_2\text{Se}_6$  and  $\text{RbTh}_2\text{Se}_6$ , showed very similar electron diffraction patterns. Figure 5 shows the electron diffraction pattern for  $\text{RbTh}_2\text{Se}_6$  with the beam perpendicular to the  $ab$  plane.<sup>31</sup> The reflections associated with the new superstructure present in  $\text{ATH}_2\text{Se}_6$  are very weak and occur along both the  $a^*$  and  $b^*$  directions with a modulation vector  $q_{\text{super}} = 0.25a^*_{\text{sub}} + 0.25b^*_{\text{sub}}$  essentially resulting in a  $4a \times 4b$  supercell. Here,  $a^*_{\text{sub}}$  and  $b^*_{\text{sub}}$  are the lengths of the reciprocal sublattice based

**Figure 5.** Selected area electron diffraction pattern with the beam parallel to the [001] zone axis from  $\text{RbTh}_2\text{Se}_6$  showing weak  $4 \times 4$  superlattice. The  $(hk0)$  family of reflections is shown. Superlattice peaks around the 310 sublattice reflection are indicated by four small arrows. Also notice that the superlattice peaks show some streaking along  $a^*$  axis due to diffuse scattering.**Chart 1.** Separation of  $\text{Se}_2^{2-}$  and  $\text{Se}^{2-}$  Groups along the  $b$  Axis and Corresponding Superstructure

on the  $\text{ATH}_2\text{Se}_6$  structure. Four weak supercell peaks around the (310) subcell reflection are indicated by small arrows in this pattern to make them more recognizable. Notice that these supercell peaks are streaking along the  $a^*$  direction due to some diffuse scattering while their shapes are sharp along the  $b^*$  direction. The streaking indicates that the superstructure in real space along the  $a$  direction is more poorly defined than along the  $b$  direction.

The substructure, observed by the X-ray diffraction analysis above represents the average positions of the Se(1) atoms. The weak superstructure seems to be caused by small displacements from the ideal local arrangement of Se(1) atoms causing the anisotropic temperature factors (in the substructure) for Se(1) to be larger. Since only  $U_{22}$  for Se(1) has an unusually high value, we expect that the positional parameters for Se(1) will vary mostly along the  $b$  axis.

On the basis of these results, we can consider a plausible superstructure model with a quadrupled cell along the  $b$  axis. If all the electrons from the alkali atoms are transferred to the diselenide groups in  $\text{ATH}_2\text{Se}_6$ , it would correspond to  $1e^-$  per two  $\text{Se}_2^{2-}$  groups, or  $2e^-$  per four  $\text{Se}_2^{2-}$  groups. Of course, two electrons can cleave, reductively, one diselenide bond into two single selenide ions,  $\text{Se}^{2-}$ . Therefore, the remaining three diselenide groups are expected to be normal  $\text{Se}_2^{2-}$  units instead of  $\text{Se}_2^{2.5-}$ , with normal bond distances and Raman frequencies. This bond cleavage, which can happen only in one out of four  $\text{Se}_2^{2-}$  groups, probably causes the CDW and the quadrupling of the  $a$  and  $b$  crystallographic axes (see tentative model in Chart 1). This model requires that all electrons are paired and thus agrees with both the diamagnetism and semiconducting nature

(30) (a) Lee, S.; Foran, B. J. *J. Am. Chem. Soc.* **1996**, *118*, 9139–9147. (b) Zhang, X.; Li, J.; Foran, B. J.; Lee, S.; Guo H.; Hogan, T.; Kannewurf, C. R.; Kanatzidis M. G. *J. Am. Chem. Soc.* **1995**, *117*, 10513–10520. (c) Lee, S.; Foran, B. J. *J. Am. Chem. Soc.* **1994**, *116*, 154–161. (d) Prodan, A.; Hla, S. W.; Marinkovic, V.; Bohm, H.; Boswell, F. W.; Bennett, J. C., *Phys. Rev. B: Condens. Matter.* **1998**, *57*, 6235–6238.

(31) (a) Since we are looking down the [001] direction, the  $hk0$  reflections which satisfy the  $h + k = 2n + 1$  condition such as 100, 010, and 210 should be systematically absent due to the extinction rule for an  $I$ -centered cell,  $hkl$ ,  $h + k + l = 2n + 1$ . The weak reflections present at these positions (where the systematic absences occur) are not violations but result from the interaction of the Ewald sphere with diffraction spots in the first-order  $[hk1]$  layer. This is due to the very thin dimensions of the observed specimens ( $<100 \text{\AA}$ ) along the crystallographic  $c$  axis which broaden the reciprocal lattice spots significantly along the  $c^*$  axis. (b) Reimer, L. *Transmission Electron Microscopy*, 2nd ed.; Springer Series in Optical Sciences; Springer-Verlag: Berlin, 1989; pp 276–284.

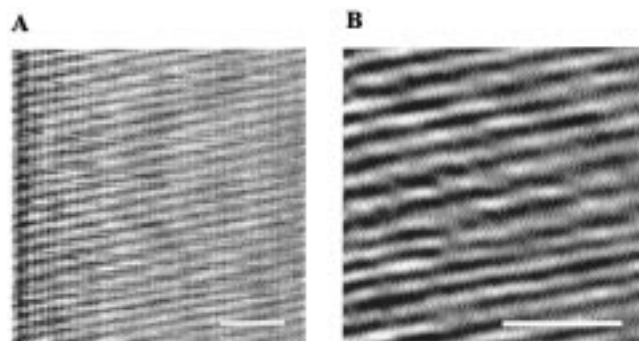
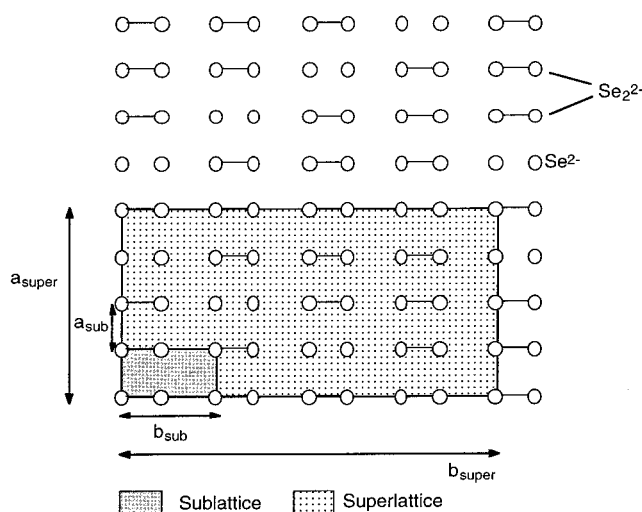


**Figure 6.** AFM image of the surface of a layer of  $\text{RbTh}_2\text{Se}_6$  corresponding to the  $ab$  plane. Panel A shows a raw image which has been flattened with a second-order polynomial to account for nonlinearity in the piezoelectric scanner. Panel B shows a blown up region of the image after a spatial Fourier filtration to remove instrumental and environmental noise from the data. The rows run parallel to the  $b$  axis. The scale bar is 20 Å.

**Chart 2.** Possible In-Plane Ordering of  $\text{Se}_2^{2-}$  and  $\text{Se}^{2-}$  Groups Consistent with the Observed Superstructure



of these compounds. It is also consistent with the Raman spectroscopic data which support the presence of single Se–Se bonds.

The quadrupling of the cell along the  $b$  axis is due to the ordering of the three  $\text{Se}_2^{2-}$  and two  $\text{Se}^{2-}$  species along this direction. The streaking of the spots along the  $a^*$  direction suggests ordering along the  $a$  direction is not as well defined as along the  $b$  direction. This can be easily understood if we consider that along the  $a$  axis direction there is no substantial interaction between the parallel  $\text{Se}_2^{2-}$  groups, since they are spaced 4.2 Å apart. Therefore, any particular ordering of the  $\text{Se}_2^{2-}$  groups and pairs of  $\text{Se}^{2-}$  atoms, along the  $a$  axis, will not have as strong of a driving force as it does along the  $b$  axis. If it occurs at all, it might be irregular and of short range. Chart 2 shows a possible  $4a \times 4b$  superstructure model with only the Se(1) atom network on the  $ab$  plane.

**Observations with Atomic Force Microscopy.** To investigate whether the  $4a \times 4b$  superstructure could be observed directly on the surface of a  $\text{RbTh}_2\text{Se}_6$  layer, we used atomic force microscopy (AFM). The AFM image of the surface of  $\text{RbTh}_2\text{Se}_6$ , shown in Figure 6A, clearly resolves the periodic rows of Se atoms in the crystals. The spacing between the rows of Se atoms were measured to be  $4.1 \pm 0.2$  Å, which corresponds well to the lattice constant in the  $a$ -direction of 4.203 Å. While the rows of Se atoms are clearly visible, we

were unable to resolve the 2.8–3 Å spacing of atoms within the rows. Figure 6B is an enhanced region of the original image, which shows a recognizable undulation along the rows of Se atoms (white regions), but no well-resolved atomic structure. It is reasonable to expect the  $\text{Se}_2^{2-}$  groups to lie slightly higher on the surface than the regions of  $\text{Se}^{2-}$  ions because of the more narrow Se–Th–Se angles associated with the diselenide groups. In this respect the higher, white, regions in the photo of Figure 6B should be due to the  $\text{Se}_2^{2-}$  groups. The average spacing of these higher lying regions seems to be  $\sim 12\text{--}15$  Å not  $\sim 24$  Å, which would be expected from the quadrupling of the lattice spacing. This discrepancy may be attributed to a certain degree of surface air oxidation of  $\text{Se}^{2-}$  ions to  $\text{Se}_2^{2-}$  groups, which will increase the density of the latter on the exposed surface. The lack of resolution along the  $b$  axis could be due to a number of factors including (a) poor definition of the superstructure along this direction, which is consistent with the observed *weak* superstructure in the electron diffraction patterns, (b) surface modification upon exposure to the ambient, or (c) limitations associated with the AFM technique. While the AFM results were consistent with the X-ray and electron diffraction data, they could not unequivocally address the issue of Se–Se bonding along the superstructure direction.

**Probing the Existence of Se–Se Single Bonds in Local Structure by Diffuse Scattering and PDF Analysis.** To determine directly the presence or absence of diselenide bonds at the normal bond distance of 2.34 Å, it is necessary to use a probe of the local structure. To do this we carried out an atomic pair distribution function (PDF) analysis of X-ray diffraction data.<sup>22,32</sup> In this technique, powder diffraction data are corrected for experimental artifacts, normalized by the photon flux and the number of scatterers, and divided by the sample-average atomic form-factor to recover  $S(Q)$ , the total scattering function (i.e., diffraction pattern) (eq 1). This is then Fourier transformed to obtain the atomic pair distribution function (PDF),  $\rho(r)$  (eq 2).

$$S(Q) = N(F_{av}(Q))^2 \left[ 1 + \int_{-\infty}^{\infty} 4\pi r^2 \rho(r) \frac{\sin Qr}{Qr} dr \right] \quad (1)$$

$$4\pi r^2 \rho(r) = 4\pi r^2 \rho_0 + \frac{2r}{\pi} \int_0^{\infty} Q[S(Q)] \sin rQ dQ \quad (2)$$

where  $Q = 4\pi \sin \theta/\lambda$ ,  $S(Q)$  = normalized scattering function,  $f$  = average atomic scattering factor,  $f_{av}(Q) = (f_K(Q) + 2f_{\text{Th}}(Q) + 6f_{\text{Se}}(Q))/(Z_K + 2Z_{\text{Th}} + 6Z_{\text{Se}})$ ,  $Z$  = atomic number,  $N$  = number of scattering atoms, and  $\rho(r)$  = atomic pair density function.

The PDF represents all the interatomic vectors in the structure. The approach is the same as has been used to study glasses and amorphous materials.<sup>22,23</sup> The PDF is a measure of the microscopic density in the solid. Recently, we have been extending its application to disordered crystalline materials,<sup>23</sup> where we can carry out a full profile-fitting regression modeling analysis, similar to Rietveld refinement, except that it yields the *local* rather than the long-range ordered structure.<sup>33</sup> In the present case, we are interested simply in determining whether short Se–Se bonds exist in  $\text{KTh}_2\text{Se}_6$  and we have not carried out a complete full profile modeling of the PDF data. This will be reported in the future.

(32) An overview of the use of this and other scattering techniques for studying disordered crystals is given in the following: Billinge, S. J. L. *Curr. Opin. Solid State Mater. Sci.* **1996**, *1*, 477.

(33) Billinge, S. J. L. *Local Structure from Diffraction*; Billinge, S. J. L., Thorpe, M. F., Eds.; Plenum: New York, 1998, in press.

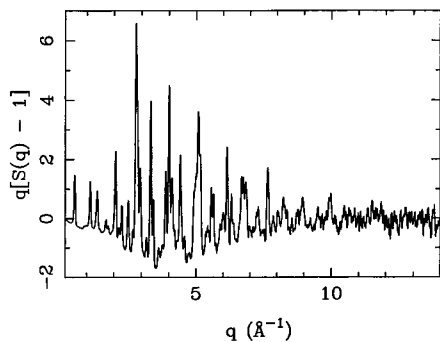


**Figure 7.** X-ray powder diffraction pattern from  $\text{KTh}_2\text{Se}_6$ . The data are shown in the form of  $Q(S(Q) - 1)$ , which is the structure function that is Fourier transformed to obtain the PDF.

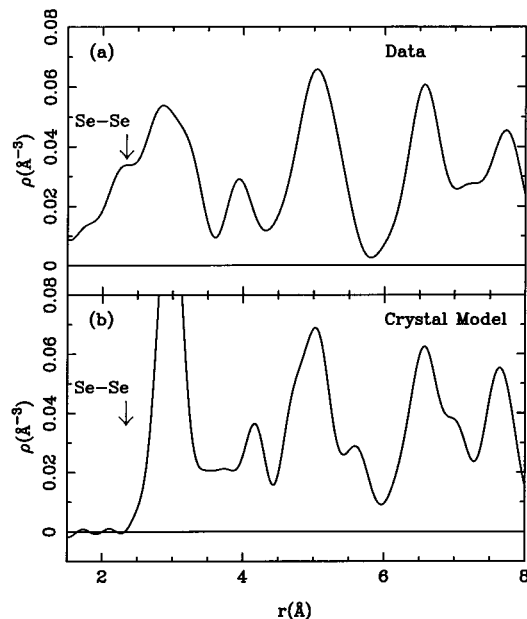


**Figure 8.** Pair distribution functions in the form of  $\rho(r)$  from  $\text{KTh}_2\text{Se}_6$ . Part a shows the PDF obtained from the data. Part b shows the PDF calculated from the crystallographic model of the structure. In both cases an arrow has been placed at a distance of 2.34 Å, which is the length expected for a diselenide bond. The lack of intensity at this position in  $\rho(r)$  for the model reflects the fact that in the average structure this distance does not exist; however, it is clear from the data that this diselenide bond *does* exist in the material.

The corrected data in the form of  $I(Q) = Q(S(Q) - 1)$  are shown in Figure 7. The data contain Bragg peaks and diffuse scattering. Both of these contributions to the scattering are Fourier transformed to obtain the PDF. This is important since the diffuse scattering contains the short-range order information which is not considered in a conventional Rietveld or single-crystal crystallographic refinement.<sup>34</sup>

Figure 8 shows PDFs in the form of  $\rho(r)$  from the data (a) and calculated from the crystal structural model (b). Overall, the PDF from the data and the model are qualitatively similar, as expected; however, there are significant differences as we describe. Peaks occur at positions,  $r$ , in  $\rho(r)$  when two atoms

(34) The data and PDF shown represent a preliminary analysis where corrections for multiple scattering and Compton scattering have not been explicitly taken into account, and the sample form factor is approximated by smoothing the data. Our experience is that these PDFs are qualitatively, though not quantitatively, correct and that this preliminary analysis will not affect the qualitative observations we are making here. A more complete analysis is in progress.

(35) Choi, K.-S.; Billinge, S. J. L.; Kanatzidis, M. G. Work in progress.

are separated by this distance in the solid. Thus, the first peak to appear is the nearest-neighbor distance. In the crystallographic model determined from the single-crystal refinement (see above), this is at 2.73 Å and is a Se–Se distance. This feature is not resolved from the strong Th–Se peak centered around 2.98 Å in the crystallographic model. This peak is the sharpest and tallest feature in the model PDF calculated from the crystallographically determined structure. The peak maximum occurs at  $0.125 \text{ \AA}^3$  and is cut off in the figure. In the model this peak is almost  $2\times$  higher than the next strongest peak at  $r = 5 \text{ \AA}$ . Also, in the crystallographically determined model, there is no intensity in  $\rho(r)$  at the position of the diselenide bond, 2.34 Å. In contrast, the PDF derived from the observed data shows that the peak at 2.98 Å is significantly broadened, to the extent that it appears weaker than the second strong peak at  $r = 5 \text{ \AA}$ . Furthermore, a well-developed shoulder is evident at 2.34 Å, indicated in Figure 8 with an arrow. These factors taken together are strong evidence for the existence of significant numbers of short diselenide bonds in the material and support the existence of the superstructure observed with the electron diffraction data (see above). A more complete modeling analysis is underway to fully determine the local arrangement of atoms in this material.<sup>35</sup>

#### 4. Conclusion

$A\text{Th}_2\text{Se}_6$  ( $A = \text{K}, \text{Rb}$ ) has a two-dimensional structure related to the  $\text{ZrSe}_3$ -type and possesses a charge density wave. The stacking arrangement of these layers is slightly modified from that of the  $\text{ZrSe}_3$  structure to accommodate the added alkali metal ions between the layers. This structure is also different from that of the telluride analogue, due to the different nature of the chalcogens. TEM and PDF studies reveal that the short Se–Se distances of 2.7 Å, determined by single-crystal X-ray diffraction, are an artifact of the averaging effect of the single-crystal structure and that there is a CDW modulation due to an extra electron from the alkali metal which cleaves one out of four diselenide bonds. The resultant structural distortion establishes a  $4a \times 4b$  superstructure due to the ordering of  $\text{Se}_2^{2-}$  groups and  $\text{Se}^{2-}$  ions. The PDF studies, which take into account the diffuse X-ray scattering in the total diffraction pattern, directly and unequivocally expose the presence of the  $\text{Se}_2^{2-}$  groups. These conclusions are supported by magnetic susceptibility measurements and optical and Raman spectroscopic data. Finally, the well-defined crystallographic sites of the  $\text{K}^+$  in the structure of  $A\text{Th}_2\text{Se}_6$  may serve as a model for the analogous sites for Li ions in  $\text{Li}_i\text{ZrSe}_3$ . The difference would be that in the latter only tetrahedral or octahedral sites would be likely, formed by the negatively charged selenium atoms from the cleaved diselenide bonds. The enhanced  $\text{Li}^+ - \text{Se}^{2-}$  interactions could stabilize the alkali metal in the interlayer space, preventing it from facile deintercalation. Finally, the observation of CDW distortion in  $A\text{Th}_2\text{Se}_6$  suggests that similar phenomena may also exist in the related  $\text{KTh}_2\text{Te}_6$  and warrants a closer look into the structure of this compound.

**Acknowledgment.** Financial support from the National Science Foundation DMR-9527347 (M.G.K.) and DMR-9633798 (S.J.L.B.) is gratefully acknowledged. M.G.K. and S.J.L.B. are A. P. Sloan Foundation Fellows. M.G.K. is a Camille and Henry Dreyfus Teacher Scholar (1993–98). This work made use of the W. M. Keck Microfabrication facility at MSU, a NSF MRSEC facility. The Siemens SMART platform CCD diffractometer was purchased with fund from the National

Science Foundation (CHE-9634638). This work made use of the SEM and TEM facilities of the Center for Electron Optics at Michigan State University.

**Supporting Information Available:** Tables of crystallographic details, atomic coordinates, isotropic and anisotropic

displacement parameters for all atoms, and interatomic distances and angles for  $\text{KTh}_2\text{Se}_6$  and  $\text{Rb}_2\text{Th}_6\text{Se}_6$  (10 pages, print/PDF). See any current masthead page for ordering information and Web access instructions.

JA981675T